Use of Full-Field DIC & IRT Measurements for the Thermomechanical Analysis of Material Behavior

André Chrysochoos, Vincent Huon, Franck Jourdan, Jean Michel Muracciole, Robert Peyroux, Bertrand Wattrisse

▶ To cite this version:

André Chrysochoos, Vincent Huon, Franck Jourdan, Jean Michel Muracciole, Robert Peyroux, et al.. Use of Full-Field DIC & IRT Measurements for the Thermomechanical Analysis of Material Behavior. Strain, 2010, 46 (1), pp.117-130. 10.1111/j.1475-1305.2009.00635.x . hal-00832297

USE OF FULL-FIELD DIC & IRT MEASUREMENTS FOR THE THERMOMECHANICAL ANALYSIS OF MATERIAL BEHAVIOR

A. Chrysochoos, V. Huon, F. Jourdan, J.-M. Muracciole, R. Peyroux, B. Wattrisse

Laboratoire de Mécanique et Génie Civil, UMR 5508 CNRS-UMII, CC 048, Place E. Bataillon, 34095 Montpellier Cedex 05, France

Phone: (+33) 4 67 143 436, Fax : (+33) 4 67 144 792
Email: surname@lmgc.univ-montp2.fr

KEY WORDS

Full-field measurements, digital image correlation, infrared thermography, thermomechanical behavior, energy dissipation, coupling heat source, stored energy, strain localization.

ABSTRACT

The paper aims to highlight the advantages of using data supplied by digital image correlation (DIC) and infrared thermography (IRT) to study the thermomechanical behavior of materials. It describes an experimental procedure for the determination of mechanical energy and heat sources involved locally during a heterogeneous tensile test. This procedure involves two complementary imaging techniques: DIC provides in-plane displacement fields while IRT enables the temperature distribution at the specimen surface to be monitored. Numerous different application examples are successively proposed to underline the promising potential of this experimental approach. Kinematical assessments can reveal the extent of homogeneity of the deformation state for a given gauge length. They can also help to determine the relevance of the variables and/or material parameters introduced in the behavioral description at the length-scale imposed by the spatial resolution of optical systems (typically 0.1 mm). Moreover, infrared and kinematical data can be used to derive heat source fields induced by the specimen loading and then to generate information on the dissipative or coupled nature of the deformation mechanisms.

INTRODUCTION

Thermal and energy effects associated with deformation processes have long been observed by researchers. The first experiments in thermoelasticity were attributed to Lord Kelvin (1880) [1-2]. The thermoelastic effects are induced by the reversible thermal dilatation of most materials. Under adiabatic conditions, they provide a direct link between temperature variations and hydrostatic stress patterns and have given rise to a wide range of applications in "thermoelastic stress analysis" (TSA). Recent application examples are given in [3-4].

The pioneering microcalorimetric tests performed by Taylor et al. (Farren and Taylor [5], Taylor and Quinney [6]) marked the beginning of work on thermoplasticity. Since that time, many researchers have worked, and continue to do so, on the problem of estimating the heat involved in irreversible mechanical transformations. In the 1970s most energy assessments were done by metallurgists. Using information on the energy balance during strain hardening, they were able to draw up models capable of estimating changes in microstructural parameters such as dislocation density, dislocation cell size, etc. An important summary work on this subject was published in 1975 by Bever et al. [7].

From a more macroscopic standpoint, over the period from 1960 to 1980, thermodynamics of irreversible processes (TIP) were increasingly used to establish material constitutive equations. Readers interested in TIP formalisms can refer, for example, to Coleman and Gurtin [8], Coleman and Noll [9], Halphen and Son [10], Germain et al. [11], and to the more recent book of Frémond [12]. TIP formalism with "internal" state variables offers a consistent and flexible framework for the description of solid material behavior. The flexibility is due to the fact that one can choose a set of internal state variables describing the macroscopic effects of complex, coupled microstructural phenomena. Mandel and Bui were among the first to show the great benefits of combining the mechanical and thermodynamic aspects of the same phenomena interpreted within a TIP framework [13-14]. In their respective work, dissipated energy during strain hardening was derived from thermocouple assessments and compared with the predictions of standard constitutive models. In the same way, the first present author developed a microcalorimeter, adapted to tensile tests, to enable overall energy balances to be performed [15-16].

It was not until the end of the 1970s that infrared techniques were used to obtain quantitative results in non-military applications. Regarding experimental investigations in the mechanics of material using digitized infrared data, the pioneering work of Saix et al. [17] and Nayroles et al. [18] should be mentioned. The first used a radiometer to observe localized plasticized zones in civil engineering metallic structures (low carbon steel) subjected to torsion loading. The second designed and used probably one of the first home-made analog-digital converters of video signals from IR cameras. Applications to polymer structures were then implemented during polycyclic tests on polyvinyl chloride [19]. Since the 1980s, the outstanding progress achieved in the electronic and computer science fields has led to the design of video signal digitization systems. Over the last 10 years, optical techniques associated with quantitative image processing have become standard. Henceforth, during a deformation process, these techniques enable operators to obtain discrete field measurements, which are essential not only to characterize and identify material behaviors but also to better distinguish between material and structure effects at an observation scale fixed by the optical systems. In the following, visible and IR systems are used: first, the visible charged-couple device (CCD) camera allows recording of speckled images and, through DIC techniques, gives access to kinematical data and enables assessment of the homogeneous character of deformation fields. Simultaneously, an infrared focal plane array (IRFPA) camera provides surface temperature fields and gives information about the dissipative nature of deformation mechanisms (viscosity of polymers, plasticity and damage of metallic materials). It also enables heat coupling sources to be identified, indicating significant thermo-sensitivity of the material and implies strong interactions between thermal and mechanical states (thermodilatability, solid-solid phase change of shape memory alloys, rubber effects of elastomers, etc.).

In addition to theoretical and numerical presentations concerning the multiscale analysis of material behavior, this paper aims to show the additional advantages of combining data supplied by two quantitative imaging techniques to analyze the energy behavior of solid materials. The definition of the different heat sources and the form of the energy balance associated with load-unload cycles are reviewed initially. Then the main features of the experimental setup and that of the electronic synchronization system linking visible with infrared image data are mentioned briefly. Finally, the majority part of the paper is devoted to highlighting the potential applications of both quantitative imaging techniques through results associated with several behavior effects: irreversibility and rate dependence associated with thermoelasticity, strain localization and hardening/softening, thermomechanical coupling and solid-solid phase change in shape memory alloys (SMAs), and necking expansion in semi-crystalline polymers. These examples were chosen to underline the role of couplings and scale effects in the understanding of deformation mechanisms.

THEORETICAL FRAMEWORK

Constitutive equations

From a thermomechanical standpoint, the deformation process is considered as a quasi-static, possibly dissipative process. The equilibrium state of each volume material element is then described using a set of N state variables: the absolute temperature T, a strain tensor ε and an N-2 element vector α which pools the so-called internal variables.

Let $\psi = e - Ts$ be the specific Helmholtz free energy, with e and s respectively being the specific internal energy and the specific entropy. The absolute temperature is by construction the partial derivative $T = e_{,s}$. The local expression of the second principle of thermodynamics leads to the Clausius-Duhem inequality [11] and allows the dissipation to be defined as:

$$d = \sigma : D - \rho\psi_{,\varepsilon} : \dot{\varepsilon} - \rho\psi_{,\alpha}.\dot{\alpha} - \frac{q}{T}.\mathrm{grad}T \geq 0\,, \qquad (1)$$

where σ is the Cauchy stress tensor, D the Eulerian strain rate tensor, ρ the mass density, and q the heat influx vector.

Constitutive state equations classically derive from the free energy potential. Under the small strain hypothesis, the strain rate is the time derivative of the strain, and the state equations read:

$$\begin{cases} s = -\psi_{,\mathrm{T}} & (a) \\ \sigma^{\mathrm{r}} = \rho\,\psi_{,\varepsilon} & (b) \\ A = \rho\,\psi_{,\alpha} & (c) \end{cases}, \qquad (2)$$

where σ^{r} is the reversible part of the stress tensor, and A is the vector gathering the conjugated variables associated with the internal state variables.

In the generalized standard material (GSM) formalism context [10], the constitutive evolution equations are derived from a dissipation potential $\varphi(\dot{\varepsilon}, \dot{\alpha}, q; T)$ and the function of the fluxes of the state variables, with T acting as a parameter. The dissipation potential must verify some convexity properties to ensure the Clausius-Duhem inequality for all (even virtual) thermodynamic processes. The partial derivatives of the dissipation potential define the complementary set of constitutive equations:

$$\begin{cases} -\dfrac{\mathrm{grad}\,T}{T} = \varphi_{,\mathrm{q}} & (a) \\ \sigma^{\mathrm{ir}} = \varphi_{,\dot{\varepsilon}} & (b) \\ X = \varphi_{,\dot{\alpha}} & (c) \end{cases}. \qquad (3)$$

They also introduce the thermodynamic forces, identified from the dissipation structure constructed as a sum of force-flux products:

$$d = \underbrace{(\sigma - \sigma^{\mathrm{r}})}_{\sigma^{\mathrm{ir}}} : \dot{\varepsilon} \underbrace{-A}_{X} . \dot{\alpha} - \frac{\mathrm{grad}T}{T} . q \geq 0 . \tag{4}$$

Property $d \equiv 0$ defines a reversible thermodynamic process. Usually the dissipation is divided into two parts that are supposed to be separately positive: the intrinsic dissipation $d_1 = \sigma^{\mathrm{ir}} : \dot{\varepsilon} + X . \dot{\alpha}$ and thermal dissipation $d_2 = -\mathrm{grad}T / T . q$. The intrinsic dissipation is associated with the material degradation while the thermal dissipation is induced by heat diffusion.

Heat equation and energy balance

The two principles of thermodynamics [11] give the following local equations:

$$\rho \dot{e} = \sigma : \dot{\varepsilon} - \mathrm{div} q + r_{\mathrm{e}} \ , \tag{5}$$

$$\rho T \dot{s} = d_1 - \mathrm{div} q + r_{\mathrm{e}} \ , \tag{6}$$

where r_{e} is a possible external heat supply (e.g. external radiation energy rate). Once it is noted that:

$$\rho T \dot{s} = -\rho T \frac{\mathrm{d}\psi_{,\mathrm{T}}}{\mathrm{d}t} = \underbrace{-\rho T \psi_{,\mathrm{TT}}}_{\rho C_{\varepsilon,\alpha}} \dot{T} - \underbrace{\rho T \psi_{,\mathrm{T}\varepsilon} : \dot{\varepsilon}}_{-\overset{\bullet}{w}_{\mathrm{the}}} - \underbrace{\rho T \psi_{,\mathrm{T}\alpha} . \dot{\alpha}}_{-\overset{\bullet}{w}_{\mathrm{thc}}} , \tag{7}$$

it is then straightforward to derive the local heat conduction equation from Eqs. (5-6). Assuming the Fourier law $q = -k \, \mathrm{grad}T$, the heat equation can be written as:

$$\rho C_{\varepsilon,\alpha} \dot{T} - \mathrm{div}(k \, \mathrm{grad}T) = \underbrace{d_1 + T \sigma^{\mathrm{r}}_{,\mathrm{T}} : \dot{\varepsilon} + T A_{,\mathrm{T}} . \dot{\alpha}}_{\overset{\bullet}{w}_{\mathrm{h}}} + r_{\mathrm{e}} \ , \tag{8}$$

where $C_{\varepsilon,\alpha}$ is the specific heat for constant ε and α, and k is the conduction tensor. The rate $\overset{\bullet}{w}_{\mathrm{h}}$ is the overall heat source induced by the deformation process. The notation $(\ )^{\bullet}$ signifies that the time variation of $(\ )$ is path-dependent, which means here that the evolved heat w_{h} is not a state function, *a priori*.

On the left side, the term $\rho C_{\varepsilon,\alpha} \dot{T}$ is the heat rate stored (or released) while $-\mathrm{div}(k \, \mathrm{grad}T)$ represents the heat losses (or heat gains) by conduction. Note that the left side is then a partial differential expression of the temperature. The different heat sources are grouped on the right side. In turn, the intrinsic dissipation d_1 is found, with the thermomechanical coupling sources showing the thermo-sensitivity of the conjugated variables σ^{r} and A, and the external heat supply r_{e}. The thermomechanical coupling sources can be split into two parts: the thermoelastic source $w^{\bullet}_{\mathrm{the}}$ due to thermoelasticity and the other thermomechanical coupling sources $w^{\bullet}_{\mathrm{thc}}$ (latent heat rate of phase change, etc). Moreover, it is worth noting that the two terms $w^{\bullet}_{\mathrm{the}}$ and $w^{\bullet}_{\mathrm{thc}}$ do not correspond respectively and systematically to the coupling terms $T\sigma^{r}_{,T}:\dot{\varepsilon}$ and $TA_{,T}.\dot{\alpha}$ but depends on the chosen set of state variables. The only general relation that can be written:

$$w^{\bullet}_{\mathrm{the}} + w^{\bullet}_{\mathrm{thc}} = T\sigma^{r}_{,T}:\dot{\varepsilon} + TA_{,T}.\dot{\alpha}\,. \tag{9}$$

If it is assumed that ρ and $C_{\varepsilon,\alpha}$ are material constants, and if the conduction tensor also remains constant and isotropic while denoting, for simplicity, k as the isotropic conduction coefficient, the heat equation can be simplified as:

$$\rho C_{\varepsilon,\alpha}\dot{T} - k\Delta T = w^{\bullet}_{\mathrm{h}} + r_{e}\,. \tag{10}$$

Energy balance for a load-unload test

Now consider a load-unload test with $\mathcal{A}=(T_{\mathcal{A}}, \varepsilon_{\mathcal{A}}, \alpha_{\mathcal{A}})$ and $\mathcal{B}=(T_{\mathcal{B}}, \varepsilon_{\mathcal{B}}, \alpha_{\mathcal{B}})$ denoting the thermomechanical states of the material at the extremities of the process. The energy balance corresponding to the following situations is illustrated in the schematic diagram proposed in Figure 1.

(i) $\mathcal{A} \neq \mathcal{B}$: this general situation is represented by a standard stress-strain diagram.

(ii) $\mathcal{A} \neq \mathcal{B}$ and $\varepsilon_{\mathcal{A}} = \varepsilon_{\mathcal{B}}$: a mechanical cycle is then associated with the load-unload test. The stress-strain diagram shows a hysteresis loop.

(iii) $\mathcal{A} = \mathcal{B}$: the mechanical cycle is now a thermodynamic cycle.

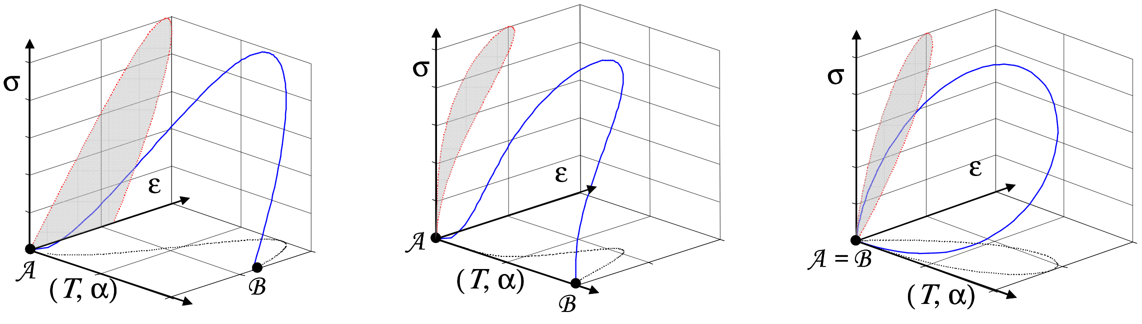

(i) *(ii)* *(iii)*

Figure 1: Schematic stress-strain diagrams for a load-unload test; $t_{\mathcal{B}}$-$t_{\mathcal{A}}$ is the cycle duration.

For quasi-static process and under the small strain hypothesis, the rate of deformation energy is classically defined by:

$$w^{\bullet}_{\mathrm{def}} = \sigma : \dot{\varepsilon} . \tag{11}$$

Through application of Eq. (4), the intrinsic dissipation d_1 is then the difference between the deformation energy rate, $w^{\bullet}_{\mathrm{def}}$, and the sum of the elastic, $w^{\bullet}_{\mathrm{e}}$, and stored, $w^{\bullet}_{\mathrm{s}}$, energy rates:

$$d_1 = w^{\bullet}_{\mathrm{def}} - w^{\bullet}_{\mathrm{e}} - w^{\bullet}_{\mathrm{s}} , \tag{12}$$

$$w^{\bullet}_{\mathrm{e}} + w^{\bullet}_{\mathrm{s}} = \sigma^{\mathrm{r}} : \dot{\varepsilon} + \mathcal{A} \cdot \dot{\alpha} . \tag{13}$$

Once again, the systematic correspondence between the terms of each side of Eq. (13) is only possible for some particular thermomechanical models.

Both principles of thermodynamics give an alternative expression of the volume deformation energy associated with the load-unload test:

$$w_{\mathrm{def}} = \int_{t_{\mathcal{A}}}^{t_{\mathcal{B}}} d_1 \,\mathrm{d}t + \int_{t_{\mathcal{A}}}^{t_{\mathcal{B}}} (w^{\bullet}_{\mathrm{e}} + w^{\bullet}_{\mathrm{s}})\mathrm{d}t = \int_{t_{\mathcal{A}}}^{t_{\mathcal{B}}} d_1 \,\mathrm{d}t + \int_{t_{\mathcal{A}}}^{t_{\mathcal{B}}} (\rho \dot{e} - \rho C_{\varepsilon,\alpha} \dot{T} + w^{\bullet}_{\mathrm{the}} + w^{\bullet}_{\mathrm{thc}})\,\mathrm{d}t , \tag{14}$$

Equation (14) shows that:

(i) In a general case the balance of deformation energy during a load-unload test involves energy dissipation, internal energy variations, variation of heat stored in the material and coupling heat sources.

(ii) For a mechanical cycle, the deformation energy then corresponds to the energy $\mathcal{A}_{\mathrm{h}}$ of the area of the hysteresis loop.

(iii) For a thermodynamic cycle, this hysteresis loop is then only due to dissipation and couplings if the volume heat capacity, $\rho\, C_{\varepsilon,\alpha}$, is assumed to be constant, i.e.:

$$w_{\mathrm{def}} = \mathcal{A}_{\mathrm{h}} = \int_{t_{\mathcal{A}}}^{t_{\mathcal{B}}} d_1 \,\mathrm{d}t + \int_{t_{\mathcal{A}}}^{t_{\mathcal{B}}} (w^{\bullet}_{\mathrm{the}} + w^{\bullet}_{\mathrm{thc}})\,\mathrm{d}t . \tag{15}$$

The energy balance form (Eq.(15)) then gives the restricted conditions for which the dissipated energy can be estimated by computing the hysteresis area of a uniaxial load-unload cycle. This underlines the necessity of analyzing the thermal effects to verify if a mechanical cycle is also a thermodynamic cycle, and checking the relative importance of coupling effects.

EXPERIMENTAL SETUP

Combining DIC & IRT data

Figure 2 illustrates the experimental set-up designed to derive local energy balances. It involves a MTS hydraulic testing machine (frame: 100 kN, load cell: 25 kN), a Cedip Jade III infrared camera and a Camelia 8M high resolution CCD camera. The optical axis of both cameras was set perpendicularly to the frame of the testing machine, and remained fixed during the test. A simultaneous record of infrared and visible images was performed on each side of the sample surface, and so thin flat samples were therefore used.

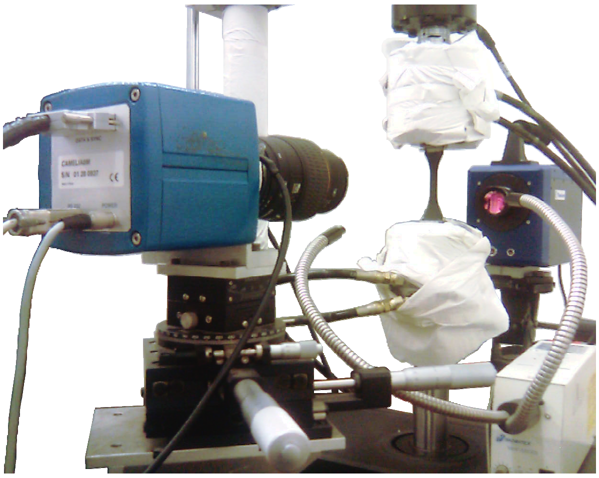

Figure 2: Experimental setup

The surface emissivity of the sample gauge part placed in front of the IR camera was increased and homogenized using a mat black paint, while the surface in front of the CCD camera was speckled with white paint on a black background to get an optimized contrast of local optical signature. Typically the size of the analyzed zone was about 20×10 mm^2 for space resolution of about 0.1 mm. The conventional strain rates were less than 10^{-2} s^{-1}. This order of magnitude of strain rate enables the quasi-staticity of processes to be ensured and induces significant (thermal) signal-to-noise ratios.

The main characteristics of the two cameras are given in Table 1.

	image size (pix.)	scale factor (µm.pix.$^{-1}$)	frame rate (Hz)
IR: Cedip Jade III	320×240	100-600	0-50
CCD: Camelia 8M	3500×2300	20-200	0-5

Table 1: Main camera characteristics

In most situations, the sample shape corresponded to a standard dog-bone specimen illustrated in Figure 3. The frame of reference used is also indicated in Figure 3.

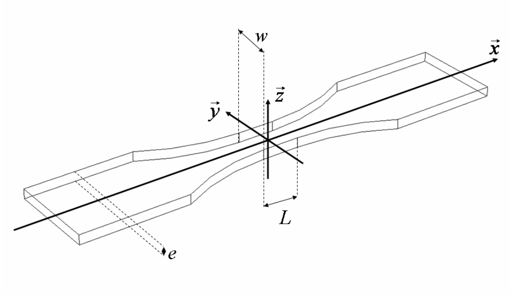

Figure 3: Specimen shape, notation and frame of reference.

Each camera was controlled by a separate computer although a specific electronic device was designed to synchronize the frame grabbing of the two cameras. The principle of the synchronization system is as follows. A frequency generator is used to produce the trigger signal of the master camera. This frequency is divided or multiplied by an integer factor to generate the trigger signal of the slave camera. Each time an image acquisition is completed, the analogue signals (stroke, load, …) provided by the testing machine sensors are digitized, and the time is given, on each acquisition computer, by a common clock having a 0.1 ms period. Using this device, the synchronization error between the two cameras is estimated to be less than 0.05 ms. Reference speckle and infrared images were mapped by determining the affine transformation coefficients (rigid body movement and homothetic transformation) of the shape of the calibrated target shown in Figure 4.

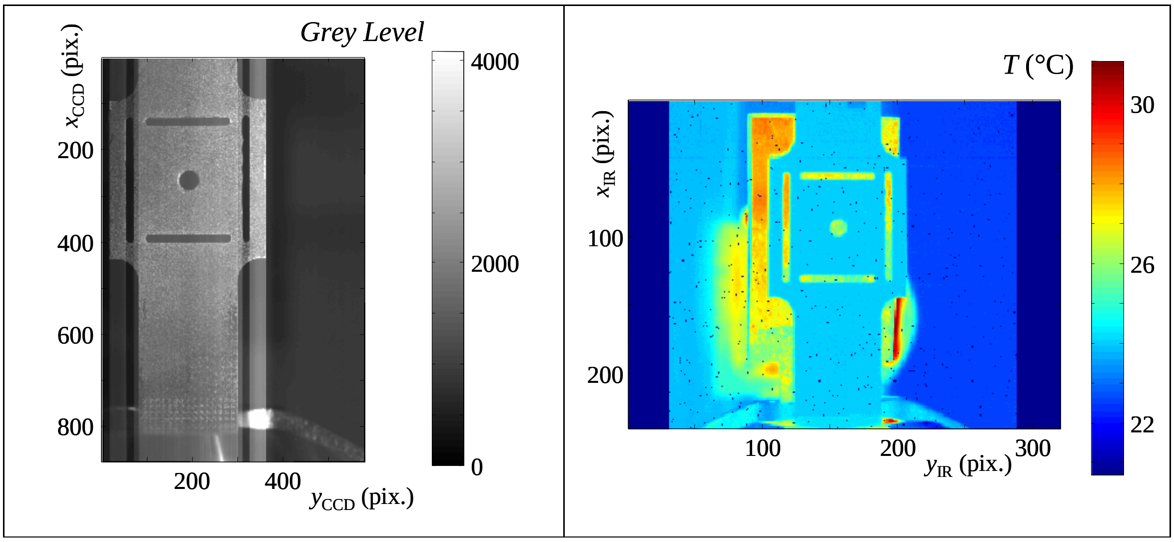

(a) (b)

Figure 4: Calibration target – (a) Visible image – (b) IR image

For each acquisition time the thermal data given by the IR camera (measured in the current, Eulerian configuration) were linearly interpolated in space and time using the positions of the deformed configuration given by the DIC computation.

This operation allowed the material surface element (*mse*) associated with the DIC mesh to be tracked so that the extent of the volume heat rate induced by matter convection and associated with the particular time derivative of the temperature could subsequently be computed and checked.

Calibration and image processing

This section briefly reviews the numerical processing principles developed to determine the different energy fields. Particular focus is given to the validation procedure improvements to check the data processing. Readers interested in the many tricky metrology problems and in a detailed presentation of image processing can refer to [20, 21], and more recently [22], where a specialized image processing technique, applied to material fatigue, is presented.

Visible images

The surface of the specimen observed by the visible CCD camera is speckled with black-white paint in order to obtain a random pattern defining the local optical signature of each *mse*. A classical digital image correlation algorithm allowed the in-plane components of the displacement field on a regular rectangular grid to be determined. The in-plane velocity and strain components were derived from the displacement data by a numerical differentiation method based on a local polynomial approximation of the displacement field. Local time fitting of displacement fields often involves a 2nd order polynomial while the local space fitting is associated with a coupled 1st order polynomial of the two in-plane coordinates [20]. The choice of approximation function and of approximation zone (*AZ*) is very important in the differentiation process. The optimized choice depends on the signal-to-noise ratio and the regularity and amplitude of the sought derivatives. The image processing then remains relevant as long as the localization zone is greater than *AZ*.

Using the kinematical data obtained by the DIC algorithm and the momentum equations, the local stress distribution was constructed, assuming a quasi-static, plane stress, isochoric transformation. Moreover, for each acquisition time t, corresponding to an applied load $F(t)$, the tensile stress σ_{xx} was assumed to be homogeneously distributed over each cross section $S(X, t)=w(X, t)\times e(X, t)$ of the specimen:

$$\sigma_{xx}(X,t)=\frac{F(t)}{S_0(X)\cdot\exp(-\varepsilon_{xx}(X,t))}, \tag{16}$$

where ε_{xx} here represents the longitudinal components of the Hencky strain. The sets (X, Y, Z) and (x, y, z) stand for the Lagrangian and Eulerian coordinates, respectively. Assuming a uniform distribution of tensile stress is naturally a strong hypothesis that may become unsound when the strain localization develops. However, the independence of ε_{xx} from the Y coordinate (*i.e.* the width direction) was confirmed by the experimental observations while the independence from the Z coordinate (*i.e.* the depth direction) was legitimated by the small sample thickness. The two other stress components (shear: σ_{xy} and contraction: σ_{yy}) were computed by integrating the momentum equations [23]:

$$\sigma_{xy}(X,Y,t)=-\frac{\partial\sigma_{xx}(x(X,Y,t),t)}{\partial x}y(X,Y,t), \tag{17}$$

$$\sigma_{yy}(X,Y,t)=\frac{\partial^2\sigma_{xx}(x(X,Y,t),t)}{\partial x^2}\cdot\left(\frac{y(X,Y,t)^2}{2}-\frac{W_0^2(X)\exp(-\varepsilon_{xx}(X,t))}{8}\right). \tag{18}$$

Eq. (17) supposes that no overall shear force occurs during the test while Eq. (18) is derived assuming a stress-free lateral surface. The deformation energy rate locally developed by the material $w_{\mathrm{def}}^{\bullet}(X,Y,t)$ was then estimated through application of Eq. (11), to give:

$$w_{\mathrm{def}}^{\bullet}=\sigma_{xx}D_{xx}+2\sigma_{xy}D_{xy}+\sigma_{yy}D_{yy}. \tag{19}$$

Thermal images

The infrared camera records the thermal radiations of the observed area. Using the pixel calibration protocol described in [24], the temperature variations of the specimen induced by the mechanical loading were deduced. To filter thermal data, a local least-squares approximation of the temperature fields was performed using the same set of polynomials as that already used for visible images. In standard conditions, the peak-to-peak thermal noise was estimated to be about 200 mK (i.e. before data filtering) and the range of the thermal noise dropped to 20 mK for standard filtering parameters.

By integrating the heat equation (8) over the sample thickness [21], and defining the mean thermal disequilibrium over the thickness between the sample and its surroundings by $\theta=\overline{T-T^{\mathrm{ref}}}$, the following 2D differential equation is obtained:

$$\rho C_{\varepsilon,\alpha}\left(\theta_{,t}+v.\mathrm{grad}\theta\right)-k\left(\theta_{,xx}+\theta_{,yy}\right)+\rho C_{\varepsilon,\alpha}\frac{\theta}{\tau_{\mathrm{th}}^{2\mathrm{D}}}=\overline{w}_{\mathrm{h}}^{\bullet}\,. \qquad (20)$$

The external heat supply r_e introduced in Eq. (5) is taken into account here by monitoring T_{ref} of an unloaded reference specimen of the same geometry placed near the specimen in the field of view of the IR camera:

$$\overline{r}_{\mathrm{e}}=\rho C_{\varepsilon,\alpha}\left(\dot{\mathrm{T}}^{\mathrm{ref}}+\frac{T^{\mathrm{ref}}}{\tau_{\mathrm{th}}^{2\mathrm{D}}}\right). \qquad (21)$$

Parameter $\tau_{\mathrm{th}}^{2\mathrm{D}}$ represents a time constant characterizing heat losses by convection and radiation between the sample surfaces and the surroundings, and $\theta_{,t}+v.\mathrm{grad}\theta$ is the particular time derivative of θ, with v representing the velocity vector.

An overall estimate of the incertitude on heat sources should take into account every possible error source associated with: (*i*) temperature accuracy, (*ii*) knowledge of the thermophysical parameters, (*iii*) relevance of the thermal modeling (heat exchanges, source distribution, averaging operation), and its identification, (*iv*) mapping between kinematic and thermal data and (*v*) image processing robustness (derivation of discrete noisy temperature fields). By limiting the error analysis to items (*i*) and (*v*), the incertitude was estimated by computing the heat source distribution from a set of IR images of a nonloaded specimen. The parasitic sources derived from the image processing then gave an order of magnitude of the absolute incertitude on the heat source fields. A mean value for a parasitic heat source on a standard steel specimen (ρ=7800 kg.m^{-3}, $C_{\varepsilon,\alpha}$ = 480 J.kg^{-}1.K^{-1}, k =40 W.m^{-1}.K^{-1}) of about 1.8 10^{-5} W.mm^{-3} was obtained, with a standard deviation of 2.7 10^{-5} W.mm^{-3}.

APPLICATION EXAMPLES

All of the following application examples stem from uniaxial loading tests. The quasi-static simple tension test is certainly one of the most widespread mechanical tests used to characterize the mechanical behavior of solid materials. The apparent simplicity of its implementation surely explains its success, but the aspects of its interpretation have already been widely mentioned in the literature. A quote from E. Orowan in 1944 [25] for instance was "*The tensile test is very easily and quickly performed but it is not possible to do much with its results because one does not know what they really mean. They are the outcome of very complicated physical processes*". Twenty-five years later, J.J. Gilman [26] wrote: "*Of all mechanical tests for structural materials, the tension test is the most common. This is true* *primarily because it is a relatively rapid test and requires simple apparatus. It is not simple to interpret the data it gives, however, as might appear at first sight*".

It is true that during quasi-static tensile loading it is often more or less implicitly assumed that:

- the state of the material is initially homogeneous at the gauge length-scale.
- the quasi-staticity of the loading implies locally quasi-static deformation processes (no local dynamic "crisis"),
- the strain field remains homogeneous throughout the gauge part of the specimen and the load is uniformly distributed over each cross-section giving rise to a uniaxial stress state, and
- the test is isothermal.

Under these assumptions it is easy to deduce from signals delivered by an extensometer and a load cell, a stress-strain diagram useful for identifying behavior models. However, this ideal situation may become unsound as soon as the sample reveals stress concentrations or strain localization zones. Besides, if the tested material somehow presents a certain degree of thermo-sensitivity, even low temperature variations may induce heterogeneous material responses just because of heat diffusion. In all of these situations, the signals of standard sensors not only characterize the material behavior but also the response of the specimen that must be henceforth considered as a structure. In other words, the experimental data can no longer be used to directly identify the behavior model, and any difference noted between theoretical predictions and experimental results requires a structural analysis that will give rise to additional difficulties. In this section, the benefits of image analysis are illustrated through several examples. Obtaining experimental measurement fields enables the material behavior and structure effects to be more accurately distinguished and helps us to a better check of the relevance of the ingredients (variables, parameters and mechanisms) introduced in the constitutive models.

Elastic-plastic transition: stress threshold and plasticity onset

The classical theory of elastoplasticity is based on the existence of an elastic domain, i.e. a convex set defined in the stress space, within which the behavior remains elastic and at the boundary of which plastic strain may develop. The uniaxial representation of this boundary is the yield stress. Figure 5 (left) shows part of the conventional stress-strain diagram of mild steel in tension. Conventional stress and strain are classically defined by $\sigma_c = F/S_0$, $\varepsilon_C = (L - L_0)/L_0$, where S_0 is the initial cross-section, while L and L_0 respectively denote the current and initial length of the sample gauge length.

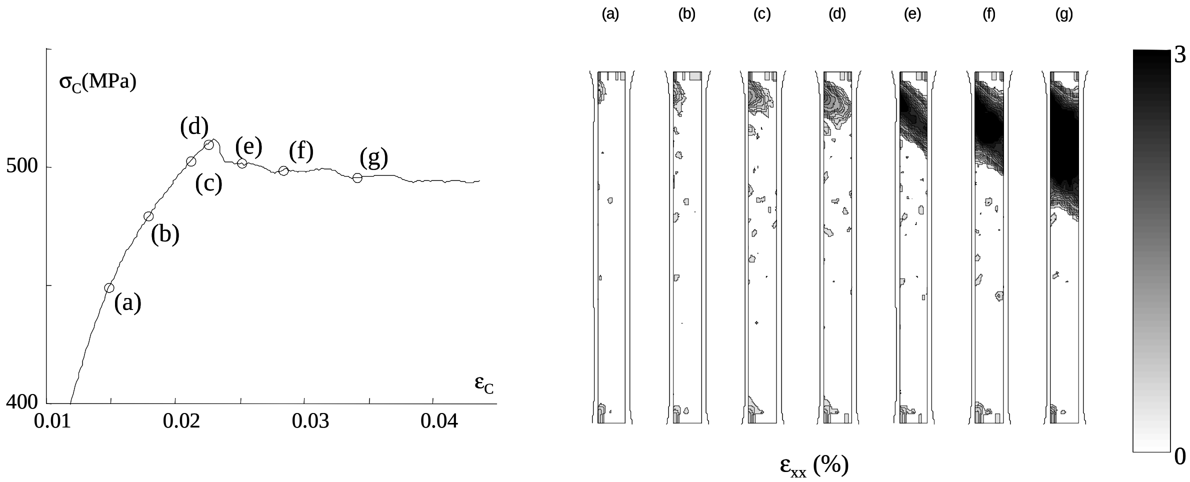

Figure 5: Monotonous tensile test of a mild steel sample;

Hencky strain is in (%)

The stress peak observed before the so-called plastic plateau is generally considered to be the yield stress. However, in Figure 5 (right), each contour plot gives the pattern of the longitudinal component ε_{xx} of the Hencky strain tensor at different steps of the tension in the Ox direction. Like other authors [27-28], the inception of strain concentration where the sample is clamped was observed (a). A localization zone then gradually develops at the top of the specimen in the Oy direction, (*b-d*), in this particular instance. From (*d*), a Lüders band propagates longitudinally throughout the sample gauge part, giving rise to the plastic plateau.

Figure 6 represents longitudinal strain-rate profiles during Lüders band propagation throughout the specimen gauge part. First, it shows that, on the optical length-scale, the strain-rate equals approximately zero outside the band.

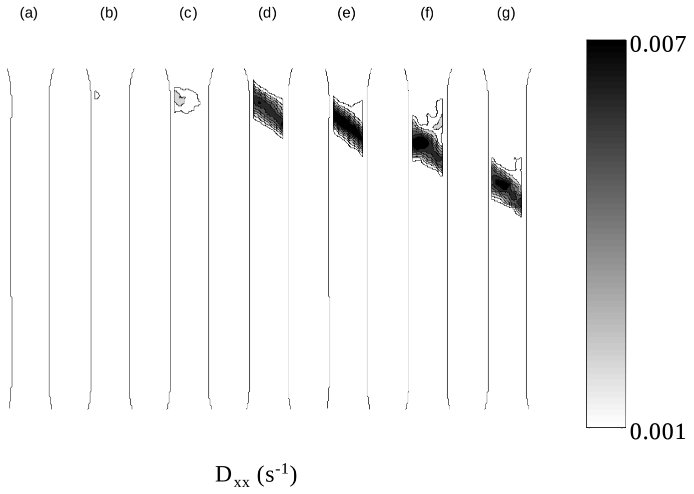

Figure 6: Distribution of the D_{xx} component of the strain-rate tensor

during longitudinal propagation of a Lüders band

Secondly, at first sight, the band propagates at a constant velocity along the sample axis. It is important to note that the apparent width of the band must not be interpreted as its real size. In fact, this width corresponds to the space covered by the band between the recording of two successive images and thus depends on the frame rate of the camera. Moreover, the measured strain-rate amplitude within the band also corresponds to that averaged between the recording of two images.

In this (classical) example, the quantitative image processing allows us to determine the difference between the yield stress of the structure and the local yield stress associated with the plasticity onset. Here, the macroscopic (structure) yield stress in tension should be about 510 MPa. The conventional stress at which the Lüders band starts developing is only 450 MPa. Both values are indeed in quite good agreement if we take into account that in the gripped regions of the sample the stress state is not purely tensile. Eqs. (16-19) were used to compute the stress patterns associated with the measured strain fields. Using the local estimate of the stress tensor, the equivalent von Mises stress σ_{eq} was derived. In Figure 7a, the σ_{eq} distribution corresponding to stage *(g)* is shown and a stress concentration in the part of the specimen affected by the Lüders band propagation is observed. To give details of the local behavior of the material, in Figure 7c the correspondence σ_{eq} vs. ε_{xx} for the points A-I located in Figure 7b are plotted. Despite the roughness of the local stress estimates, the yield stress is approximately the same for all the points considered and that it corresponds to the overall peak stress. As it does not appear in the local responses, this stress peak is consequently interpreted as a structure effect due to the lateral Lüders band development while the plateau corresponds to the longitudinal propagation.

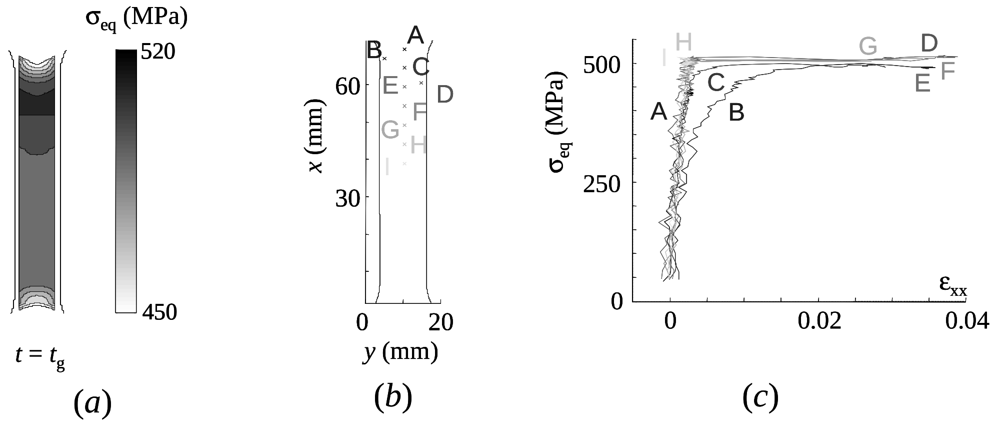

Figure 7: von Mises stress distribution associated with the propagation of a Lüders band. *(a)* stress pattern at stage *(g)* , *(b)* chosen *mse*; *(c)* local σ_{eq} vs. ε_{xx} responses.

Thermoelastic coupling and time-dependence

In the GSM framework [11, 12], the elastic domain can be extended to a convex domain in the space of the thermodynamic forces associated with the state variable set chosen to describe the material behavior.

If the deformation process is considered as purely thermoelastic, the material gives rise to the famous thermoelastic effects already mentioned. In this context, no intrinsic dissipation occurs, with the internal state variables α being fixed within the elastic domain. The only heat source induced by the deformation is consequently the thermoelastic coupling source. The presence of such a coupling implies a rate dependence of the material behavior. To justify this assertion the thermomechanical formalism previously introduced is applied in an academic 1D situation.

In the following thermoelastic model, if the chosen state variables are the absolute temperature T and the small longitudinal strain ε, the free energy can be written as:

$$\rho\psi\left(T,\,\varepsilon\right)=\frac{1}{2}E\varepsilon^{2}-E\lambda_{\mathrm{th}}(T-T_0)\varepsilon-\rho s_0(T-T_0)-\rho C\left(T\,\mathrm{Log}\frac{T}{T_0}-(T-T_0)\right),\tag{22}$$

where T_0 is the equilibrium temperature and s_0 is the entropy of the reference equilibrium state. We suppose that the mass density ρ, the specific heat C, the thermal dilatation coefficient λ_{th} and the Young modulus E are material constants. Applying Eq. (2) the specific entropy and the reversible stress are then:

$$s=-\psi_{,T}=s_0+\frac{E\lambda_{\mathrm{th}}}{\rho}\varepsilon+C\,\mathrm{Log}\frac{T}{T_0},\tag{23}$$

$$\sigma^{\mathrm{r}}=\rho\psi_{,\varepsilon}=E\left(\varepsilon-\lambda_{\mathrm{th}}(T-T_0)\right).\tag{24}$$

For pure thermoelastic transformations, the only irreversibility is then due to the heat diffusion. The dissipation potential can then be chosen as:

$$\varphi\left(\dot{\varepsilon},q;\,T\right)=\frac{1}{2T}q.k^{-1}q\,.\tag{25}$$

Equation (3) gives the irreversible stress and the heat influx form:

$$\sigma^{\mathrm{ir}}=\varphi_{,\dot{\varepsilon}}=0\,,\tag{26}$$

$$-\frac{\mathrm{grad}T}{T}=\varphi_{,q}=\frac{k^{-1}q}{T}.\tag{27}$$

Through application of Eqs (5 and 17-19), the heat diffusion equation becomes:

$$\rho C\dot{T}-k\Delta T=-E\lambda_{\mathrm{th}}T\dot{\varepsilon}\;.\tag{28}$$

To avoid solving a boundary value problem, a property derived from the spectral analysis of the heat diffusion equation is used in the case of the homogeneous heat source distribution and linear boundary conditions (Fourier's condition). In such a situation, Ref. [21] showed that the spectral solution of the heat diffusion problem can be well approximated by the first eigen function of the Laplacian operator, implying that the local volume heat losses are, in a first approximation, proportional to the thermal disequilibrium θ:

$$-k\Delta T \approx \rho C \frac{T - T_0}{\tau_{\mathrm{th}}} = \rho C \frac{\theta}{\tau_{\mathrm{th}}}, \tag{29}$$

where τ_{th} is a time constant characterizing the heat losses. The main equations of the thermoelastic problem can then be summed up by the following coupled algebraic and differential equations:

$$\begin{cases} \sigma = E(\varepsilon - \lambda_{\mathrm{th}}\theta) & (a) \\ \dot{\theta} + \dfrac{\theta}{\tau_{\mathrm{th}}} = -\dfrac{\lambda_{\mathrm{th}} E (T_0 + \theta)\dot{\varepsilon}}{\rho C} & (b) \end{cases} . \tag{30}$$

Consider a cyclic strain-controlled test for which the strain is the harmonic signal $\varepsilon = \varepsilon_0 \sin(2\pi f_{\mathrm{L}}\, t)$, where ε_0 is the strain amplitude and f_{L} the loading frequency. One experimentally observes, after some cycles, that the temperature variations become progressively periodic and symmetric with respect to the time axis. This transient effect corresponds to the general homogenous solution of the differential equation Eq. (30b). Once the periodic regime is reached, the mechanical cycles become thermodynamic cycles and the hysteresis area A_{h}, according to equation Eq. (13), reads:

$$w_{\mathrm{def}} = A_{\mathrm{h}} = \int_t^{t+f_{\mathrm{L}}^{-1}} \dot{w}_{\mathrm{the}} \mathrm{d}\tau = w_{\mathrm{the}} \tag{31}$$

Isothermal processes correspond to significant heat losses ($\tau_{\mathrm{th}} \rightarrow 0$) or negligible coupling sources (*i.e.* low loading frequency, $\frac{\rho C}{\lambda_{\mathrm{th}} T_0 E \varepsilon_0} \tau_{\mathrm{th}}^{-1} \gg f_{\mathrm{L}}$). Conversely, adiabatic processes are obtained for small heat losses ($\tau_{\mathrm{th}} \rightarrow \infty$) and significant coupling sources (*i.e.* high loading frequency $\frac{\rho C}{\lambda_{\mathrm{th}} T_0 E \varepsilon_0} \tau_{\mathrm{th}}^{-1} \ll f_{\mathrm{L}}$). For isothermal or adiabatic situations, the hysteresis area vanishes.

In nonadiabatic and nonisothermal situations, the thermoelastic coupling induces rate dependence. It is interesting to consider the rate dependence by writing a rheological equation. From Eq. (30), substituting the temperature, in the case of small thermal variations ($\theta \ll T_0$), gives:

$$\sigma + \tau_{\mathrm{th}} \dot{\sigma} \approx E\varepsilon + E\tau_{\mathrm{th}} \left(1 + \frac{E\lambda_{\mathrm{th}}^2 T_0}{\rho C}\right)\dot{\varepsilon} \tag{32}$$

This rheological equation looks similar to ones obtained in linear viscoelasticity, which naturally complicates the behavior analysis. For instance, for some visco(thermo)elastic polymers, the thermoelastic source intensity may be significantly greater than the dissipation intensity [29]. For such materials, the results, given by standard visco-analysis and based on the determination of complex moduli, are more difficult to interpret because of the superimposition of two similar independent time effects respectively induced by viscous dissipation and thermoelastic coupling.

Elastic cyclic loading of dissipative structures

The approximation underlying the existence of an elastic domain becomes unsound as soon as a large number of “elastic” cycles are performed. Indeed, for crystalline materials, dislocations oscillate slightly, even under low cyclic stress amplitudes. Cycle by cycle, dislocations gradually gather to build up persistent slip bands (PSB), which are microscopic zones where the plasticity develops preferentially inside some “well” oriented grains [30]. This microplasticity development finally leads to microcracks followed by a sudden rupture. This is the so-called high cycle fatigue (HCF) of materials and it has become essential to master the kinetics of this phenomenon in industrial applications for obvious economical and safety reasons. The HCF analysis of materials and structures currently involves a large number of research centers all over the world. It has been recently shown that the thermomechanical approach could be beneficially applied to gain further insight into fatigue kinetics [33-34]. From the image processing standpoint, the main difficulty was to extract low dissipation intensities from large thermoelastic source amplitudes. Readers interested in the use of quantitative imaging techniques applied to the analysis of fatigue mechanisms can refer to [22], where the infrared image processing developed to process fatigue tests is detailed. Results of applications to steel and aluminum can also be found in [31-33], and more recently in [34] where energy balance distributions were constructed using DIC and IRT techniques. To give a brief illustration of the potentiality of the image analysis, Figure 8 shows the mean dissipation pattern per cycle $\tilde{d}_1$ calculated at different stress ranges. During a block of 20000 cycles, this heterogeneous pattern remains constant as long as a fatigue crack does not initiate.

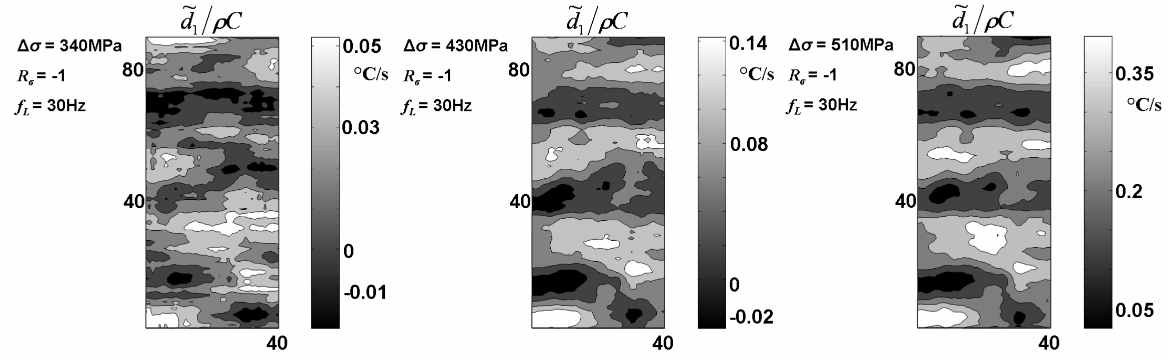

Figure 8: Dissipation intensity versus stress range (from [33]).

The contour plots in Figure 8 also show that areas where the dissipation is high (respectively low) remain approximately the same from one block to another, even if the dissipation naturally increases with the stress range. During a (last) loading block, a localized zone of high dissipation several hundreds of cycles before crack onset was observed. Moreover, it was also noted that this zone always corresponded to a candidate zone where the dissipation level was high from the beginning of the fatigue test (i.e. for low stress ranges.)

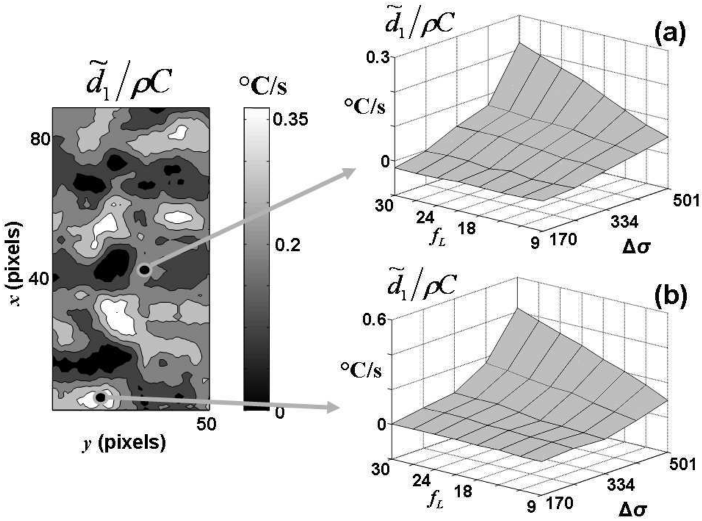

Figure 9: Dissipation patterns within two different material zones (from [33]).

Besides, Figure 9 shows examples of dissipation variations associated with zones of the same specimen as a function of $\Delta\sigma$ and f_L. During this test performed at R_σ=-1, $\Delta\sigma$ increased from 170 to 500 MPa and f_L increased from 9 up to 30 Hz for each load level. Dissipation values in the first location (Figure 9a) are twofold lower than that measured in the second area (Figure 9b). First, the shape of both surfaces $\tilde{d}_1(\Delta\sigma, f_L)$ is clearly very similar. At constant stress, it can also be underlined that $\tilde{d}_1$ increases in a quasi-linear way with the load frequency f_L for both zones and for all stress ranges. This linearity of $\tilde{d}_1$ with f_L is then consistent with an interpretation of the fatigue mechanisms in terms of time-independent microplasticity.

Hardening and softening: material or structure effect?

Strain hardening and softening are essential factors in the mechanical behavior description. They are systematically mentioned in the construction of instability criteria for the detection of localization onset [35, 36]. They are also omnipresent in problems of solid-solid phase change where the non-monotonous correspondence between stress and strain is a basic component of numerous phase transition theories [37, 38]. The examples shown hereafter question the intrinsic character of strain softening. The first one presents the early and gradual development of strain localization during monotonous tensile tests for common stamping steel (European grade: DD14) [39]. The second shows the conventional stress-strain diagram of a semi-crystalline polymer (PA12) characterized by strain softening followed by a plateau [40].

To simplify the data interpretation, contour plots were chosen for quick viewing of the phenomenon patterns. Space-time charts were then constructed with the abscissa axis (bottom) representing the time and the ordinate axis (left), the longitudinal sample axis. Using the displacement data, a Lagrangian representation of profiles has been proposed. A conventional stress-strain diagram was superimposed to give the reader a familiar benchmark to link the local pattern of the measurements to the loading state of the sample (right/top).

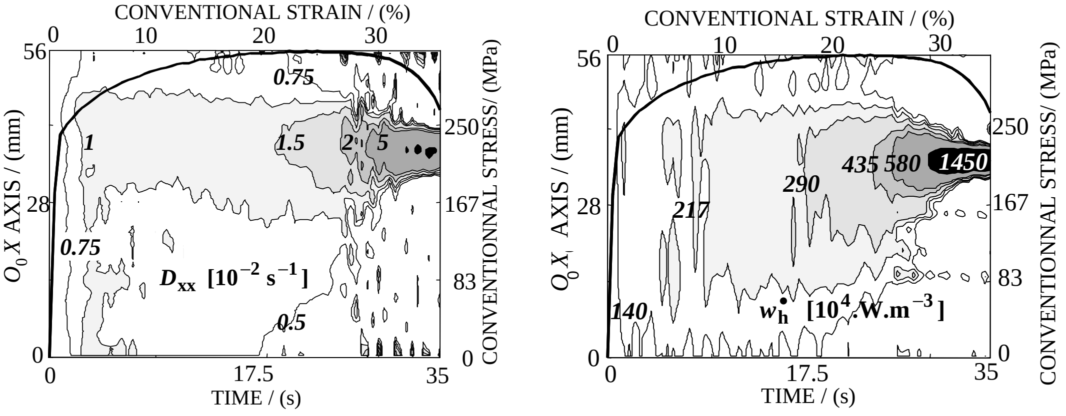

(a) (b)

Figure 10: Spatiotemporal patterns of (a) $D_{xx}(t, X, Y = 0)$, (b) $w_h^\bullet(t, X, Y = 0)$

Case of DD14 steel (from [23]).

Figure 10a shows the spatiotemporal patterns of the strain-rate component D_{xx}. The conventional strain-rate amplitude $d\varepsilon_c/dt$ is about 10^{-2} s^{-1}. This value can be compared with those of the different level curves. At the beginning of the test, D_{xx} is less than $d\varepsilon_c/dt$ throughout the test section because of the elasticity of the testing machine frame. The early and steady narrowing of the curves indicates that the region where the strain-rate amplitude is highest concentrates gradually long before the maximum load is reached. Therefore the locus where the sample fracture will take place can already be detected while the sample still hardens. These results suggest that diffuse and localized necking are two concurrent aspects of the same phenomenon. In practice, it would then be difficult to establish a definite boundary between these two *localization modes*. In the same way, Figure 10b shows the distribution of heat sources. Cross-sections where the strain rate is the highest are sites where the mechanical energy is preferentially dissipated. The calorimetric data then confirms the heterogeneous character of the deformation process. Consequently, the sample gauge part can no longer be considered as a representative elementary volume of the material behavior.

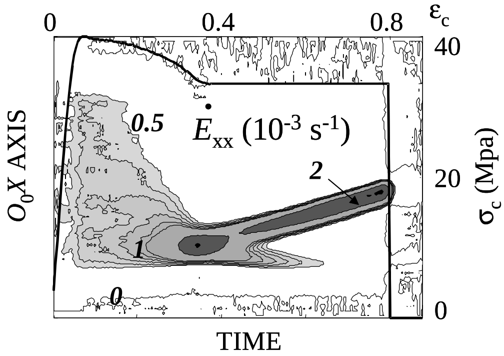

Figure 11: Spatiotemporal pattern of $D_{xx}(t, X, Y = 0)$.

Case of Polyamide 12 (from [40]).

Figure 11 gives another example in the case of a semi-crystalline polymer. This represents the longitudinal distribution of the Green-Lagrange strain-rate component $\dot{E}_{xx}$ according to the loading direction. The concentration of level curves indicates progressive localization of the deformation that appears after the yield stress and induces softening that is observable in the conventional stress-strain curve. Propagation of the localization zone then gives rise to the plateau (elongation at constant load), which corresponds to the displacement of necking lips throughout the sample gauge part.

Solid-solid phase change: another coupling effect

As already underlined above, the rate-dependence of the material behavior is often implicitly associated with viscous effects for which the stress intensity is directly related to the strain-rate amplitude. This rate-dependence can be detected by classical creep and relaxation tests. Besides, for mechanical cyclic tests, as already mentioned, the rate-dependent material exhibits stress-strain hysteresis loops. The classical example of thermoelasticity showed that some materials may present strain-rate sensitivity without actually being viscous. Another example is given by shape memory alloys (SMAs) which also present such behavior in a given stress and temperature domain. This behavior is qualified as *pseudoelastic*: *elastic* because strains are generally recoverable when the sample is unloaded, *pseudo* because the stress-strain relationship is not a map-to-map correspondence (hysteretic behavior). This unique behavior is due to the austenite-martensite phase change induced by thermomechanical loading. This transition occurs within a given domain of the stress-temperature space called the transition domain. At the microstructural level, this first-order phase transition corresponds to a change in the crystallographic networks and is accompanied by latent heat. Since the composition of the phase mixture is particularly sensitive to stress and temperature variations, a stress-induced phase transition is automatically disturbed by temperature variations induced by the latent heat. This strong coupling of thermal and mechanical states leads to a time-dependent mechanical behavior inasmuch as the temperature variations are also governed by heat diffusion mechanisms and not only by loading parameters. The data shown hereafter are derived from experiments performed on a monocrystalline CuZnAl SMA, [41, 42]. In this work only monocrystalline round bars were available and then tested. The IR camera was solely used and limited to the capture of longitudinal thermo-profiles. The conventional stress and strain were classically derived using the load and stroke signals, respectively.

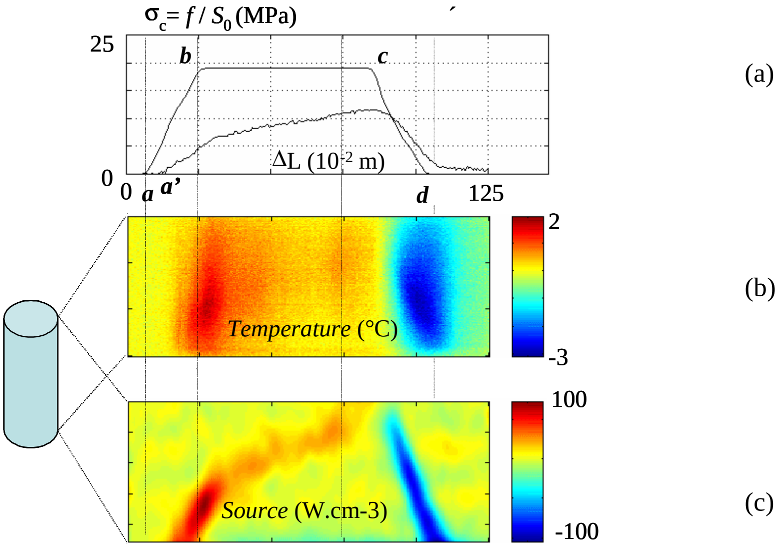

Figure 12: Propagation of a phase change front in a CuZnAl monocrystal, (from [41]).

Figure 12a presents a load-controlled test divided into three parts: a loading stage (*a-b*), a holding stage at constant stress (*b-c*), an unloading stage (*c-d*). Variations in the temperature profile along one generatrix of the cyclindric sample are presented in Figure 12b. In the same way, the corresponding heat sources are plotted in Figure 12c. The first part (*a-a'*) of the loading stage is associated with the elastic behavior of the material, involving small temperature variations and slight deformation of the sample.

At time *a'*, strong positive heat sources concentrate at the bottom of the sample in a zone that shifts during loading (*a'*-*b*). The displacement of this zone is associated with the propagation of a phase change front (austenite/martensite exothermal transformation). When the stress is held (*b*-*c*), sources of lower intensity are observed and the zone where they concentrate moves more slowly. The associated phase transformation also involves localized strain and then creep of the sample. Finally, during the unloading stage (*c*-*d*), we observe the propagation of a zone where negative sources are concentrated (martensite/austenite endothermal transformation). Note that the localized character of the transformation is less obvious when assessing the thermal data (Figure 12b) because of the regularizing effect of heat diffusion. It is heat diffusion combined with the phase change mechanism (strong coupling) that induces the rate dependence. To verify this assertion, the experiments shown in Figure 13 were performed.

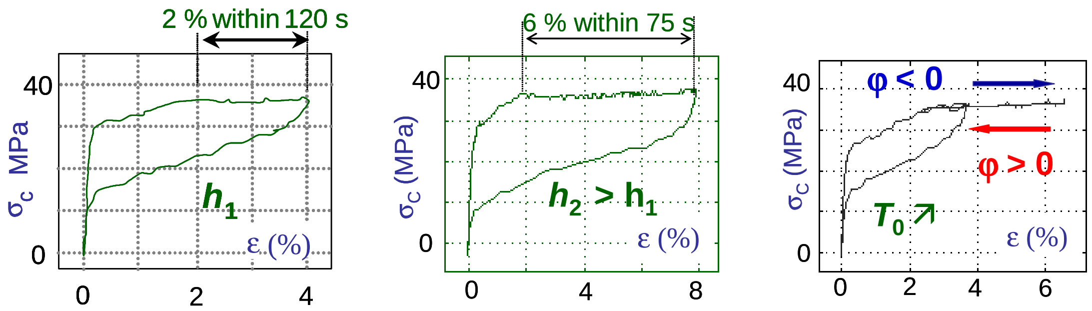

(a) (b) (c)

Figure 13: Influence of heat exchange on the mechanical response of a pseudoelastic SMA: (a) natural convection, (b) light turbulent convection, (c) inversion of heat exchange by increasing T_0.

Figure 13a and 13b shows the mechanical responses obtained with two different heat fluxes exchanged between the sample and the surroundings (symbolized by the heat exchange coefficient *h*). In practice, the flux is increased by putting an electric fan in front of the sample. The creep, observed when the stress is kept constant, is induced by propagation of the front, whose direction is related to heat exchanges. The band propagates faster as the intensity of the heat flux at the sample boundary increases. It is even possible to invert the phase change pattern ("reverse" creep!) by reversing the sign of the heat exchanged flux (Figure 13c). To perform this heat flux reversion, a spotlight was used to warm the surrounding air.

CONCLUDING COMMENTS

The aim of this paper was to show the richness of the experimental information which is now provided by quantitative imaging techniques to characterize and identify the behavior of materials and engineering structures. The importance of the scale at which these measurements were performed is also stressed and the consequences on their interpretation in terms of material properties or interactions between material and geometrical effects. The combined use of DIC and IRT enabled the local energy balance to be derived. In particular, the determination of the heat source which accompanies the deformation process is critical. Thermodynamic analysis of the energy balance showed the influence of dissipated and thermomechanical coupling mechanisms on the stress-strain response, which gave precious information on the nature and the evolution of deformation mechanisms. The results presented in the text successively and briefly approached the concepts of elastic threshold and plastic plateau, the scale dependence of the hardening/softening behavior, the effects of time and the existence of mechanical hysteresis loops induced by coupling mechanisms and heat diffusion. For each application example, the results presented are concerned only with observations at the meso- and macroscopic scales, during uniaxial loadings at room temperature. The constant progress achieved in the field of optical metrology allowed us to consider the use of kinematic and calorimetric full field measurements at finer observation scales. These data will be useful for testing the efficiency of homogenization methods to take thermomechanical effects observed at microscopic scales into account. Lastly, the development of rapid cameras also makes it possible to consider extension of the imaging techniques to dynamic loading at high temperature, where the dissipative and coupling effects are surely essential in the understanding of deformation mechanisms.

REFERENCES

1. Thomson, W. (Lord Kelvin) (1853) On the thermoelastic and thermomagnetic properties of matter, *Trans. Roy. Soc. Edinb.*, 20, (161), 57-77.
2. Thomson, W. (Lord Kelvin) (1857), On the dynamical theory of heat, with numerical results deduced from Mr Joule's equivalent thermal unit, *Quart. J. of Pure and Appl. Math.*, 1, (57), 261-288.
3. Dulieu-Barton, J.M., Eaton-Evans, J., Little, E.G. and Brown, I.A. (2008) Thermoelastic analysis of high pressure angioplasty balloons. *Strain*, 44, (1), 102-118.
4. Sathon, N. and Dulieu-Barton, J.M. (2007) Evaluation of sub-surface stresses using thermoelastic stress analysis. *Applied Mechanics and Materials*, 7-8, 153-158.

5. Farren, W. and Taylor G. I., (1925) The heat developed during plastic extension of metals, *Proc. Roy. Soc. London.*, part A, 107, 422-451.

6. Taylor, G. and Quinney, H, (1934) The latent energy remaining in a crystal after cold working, *Proc. Roy. Soc. London*, part A, 143, 307-325.

7. Bever, M.B, Holt, D.L and Titchener, A.L. (1973) The stored energy of cold work, *Progress in Materials Science*, 1st Ed. Pergamon Press Ltd, Oxford.

8. Coleman, B. and Gurtin, M. (1967) Thermodynamics with internal state variables, *The J. of Chem. Phys.*, 47, (2), 597-613

9. Coleman, B. and Noll, W. (1963) The thermodynamics of elastic materials with heat conduction and viscosity, *Arch. Rat. Mech.*, (13), 167-178.

10. Halphen, B. and Nguyen, Q. S, (1975) Sur les matériaux standards généralisés, *J. Méc.*, 14, (1), 39-63.

11. Germain, P., Nguyen, Q. S and Suquet, P. (1983), Continuum Thermomechanics, *J. Appl. Mech.*, 50, (4B), 1010-1020.

12. Frémond, M. (2002), Non-smooth Thermomechanics, Springer, Berlin.

13. Mandel, J (1965) Energie élastique et travail dissipé dans les modèles, *Cahiers du Groupe Français de Rhéologie*, 1, (1), 9-14.

14. Bui, H. D. (1965) Dissipation d'énergie dans une déformation plastique, *Cahiers du Groupe Français de Rhéologie*, 1, (1), 15-19.

15. Chrysochoos, A. (1985) Energy-balance for elastic-plastic deformation at finite strain, *J. Mec. Théo et Appl.*, 4, (5), 589-614.

16. Chrysochoos, A. and Martin, G. (1989) Tensile test microcalorimetry for thermomechanical behaviour law analysis, *Mat. Sci. and Eng. A*, 108, 25-32.

17. Saix, C. and Jouanna, P. (1980) Analyse de la dissipation plastique par thermographie de surface, résultats expérimentaux et modélisation, *Rev. Roum. Sci. Tech.- Mec. Appl.*, T 25, (5), 203,719.

18. Nayroles, B., Bouc, R., Caumon, H., Chezeaux, J.-C. and Giacometti, E. (1981) Téléthermographie infrarouge et mécanique des structures, *Int. J. Engng. Sci.*, 19, (7), 929-947.

19. Brémond, P., (1982), Développement d'une instrumentation infrarouge pour l'étude des structures mécaniques, PhD thesis, Marseille University, France.

20. Wattrisse, B., Chrysochoos, A., Muracciole, J.-M. and Nemoz-Gaillard, M. (2000) Analysis of strain localization during tensile test by digital image correlation, *J. Exp. Mech.*, 41, (1), 29-38.

21. Chrysochoos, A. and Louche, H. (2000) An infrared image processing to analyze the calorific effects accompanying strain localisation, *Int. J. of Engng. Sci.*, 38, 1759-1788.

22. Berthel, B., Chrysochoos, A., Wattrisse B. and Galtier, A. (2008) Infrared image processing for the calorimetric analysis of fatigue phenomena, *Exp. Mech.,* 48, (1), 79-90.

23. Wattrisse, B., Chrysochoos, A., Muracciole J.-M. and Nemoz-Gaillard, M. (2001) Kinematic manifestations of localisation phenomena by image correlation, *Eur. J. Mech., A/solids*, 20, 189-211.

24. Honorat, V., Moreau, S., Muracciole, J.-M., Wattrisse, B. and Chrysochoos, A. (2005) Calorimetric analysis of polymer behaviour using a pixel calibration of an IRFPA camera, *Int J. on Quantitative Infrared Thermography*, 2, (2), 153-172.

25. Orowan E. (1944) Discussion on the significance of tensile and other mechanical test properties of metals, *Proc. Instn. Mech. Engrs (GB)*, discussion paper, meeting in London on Friday, 18th June 1943, 151, 131-146.

26. Gilman, J.J. (1969), Micromechanics of flow in solids, McGraw-Hill, New-York.

27. Hähner, P. (1994) Theory of solitary plastic waves, part I: Lüders band in polycrystals, *Appl. Phys.*, A58, 41-48.

28. Zaiser, M. and Hähner, P. (1997) Oscillatory modes of plastic deformation: theoretical concepts, *Phys. Stat. Sol. (b)*, 199, 267-330.

29. Moreau, S, Chrysochoos, A., Muracciole, J.-M. and Wattrisse, B. (2005) Analysis of thermoelastic effects accompanying the deformation of PMMA and PC polymers, *C. R. Acad Sci*, 333, (8), 648-653.

30. Mughrabi, H. (1983) Dislocation wall and cell structures and long range internal stresses in deformed metal crystals, *Acta Metallurgica*, 31, (9), 1367-1379.

31. Boulanger, T., Chrysochoos, A., Mabru, C. and Galtier, A. (2004) Calorimetric and thermoelastic effects associated with the fatigue behavior of steels, *Int. J. of Fatigue*, 26, 221-229.

32. Morabito, A.E., Chrysochoos, A., Dattoma, V. and Galietti, U. (2007) Analysis of heat sources accompanying the fatigue of 2024 T3 aluminium alloys, *Int. J. of Fatigue*, 29, (5), 977-984.

33. Berthel, B., Galtier, A., Wattrisse, B. and Chrysochoos, A. (2007) Thermographic analysis of fatigue dissipation properties of DP60 steel, *Strain*, 43, 273–279.

34. Chrysochoos, A., Berthel, B., Latourte, F., Pagano, S., Wattrisse, B. and Weber, B. (2008) Local energy approach to fatigue of steel, *Strain*, 44, 327–334.

35. Hill, R. (1958) A general theory of uniqueness and stability in elastic-plastic solids, *J. Mech. Phys. Solids*, 6, 236-249.

36. Rudnicki, J.W. and Rice, J.R. (1975) Conditions for the localization of deformation in pressure sensitive dilatant materials, *J. Mech. Phys. Solids*, 23, 371-394.

37. Ericksen, J.L. (1991) Introduction to Thermodynamics of Solids, Applied Mathematics and Mathematical Computation 1, Chapman & Hall, 3, 39-82.

38. Abeyaratne, R. and Knowles, J.K. (1993) A continuum model of thermoelastic solid capable of undergoing phase transitions, *J. Mech. Phys. Solids*, 41, 541-571.

39. Chrysochoos, A., Muracciole, J.-M. and Wattrisse, B. (2000) Experimental analysis of strain and damage localization, Proc. *Symposium on continuous damage and fracture*, Cachan, Ed. A. Benallal, , 41-51.

40. Wattrisse, B., Muracciole, J.-M. and Chrysochoos, A. (2001) Thermomechanical effects accompanying the localized necking of semi-crystalline polymers, *Int. J. of. Therm. Sci.*, 41, 422-427.

41 Balandraud, X., Chrysochoos, A., Leclercq, S. and Peyroux, R. (2001) Effet du couplage thermomécanique sur la propagation d'un front de changement de phase", *C.R. Acad. Sci.*, 329, 621-626.

42 Chrysochoos, A., Licht, C. and Peyroux, R. (2003) A one-dimensional thermomechanical modeling of phase change front propagation in SMA monocrystal, *C. R. Acad. Sci.*, 331, 25-32.